

# Revisiting Bondi-Hoyle-Lyttleton accretion in binary systems

EMILIO TEJEDA<sup>1</sup> AND JESÚS A. TOALÁ<sup>2</sup>

<sup>1</sup>CONAHCyT - Instituto de Física y Matemáticas, Universidad Michoacana de San Nicolás de Hidalgo, Ciudad Universitaria, 58040 Morelia, Mich., Mexico

<sup>2</sup>Instituto de Radioastronomía y Astrofísica, Universidad Nacional Autónoma de México, Morelia 58089, Mich., Mexico

Submitted to ApJ

## ABSTRACT

The Bondi-Hoyle-Lyttleton (BHL) accretion model is widely used to describe how a compact object accretes material from a companion's stellar wind in binary systems. However, this classical model becomes inaccurate when the wind velocity ( $v_w$ ) is comparable to or less than the orbital velocity ( $v_o$ ), predicting nonphysical accretion efficiencies above unity. This limits its applicability to systems with low wind-to-orbital velocity ratios ( $w = v_w/v_o \leq 1$ ), such as symbiotic systems. We revisit the BHL model and introduce a geometric correction factor that accounts for the varying orientation of the accretion cylinder relative to the wind direction. This correction ensures physically plausible accretion efficiencies ( $\eta \leq 1$ ) for all  $w$  in circular orbits. Our modified model naturally predicts the flattening of the accretion efficiency observed in numerical simulations for  $w < 1$ , without the need for *ad hoc* adjustments. We also peer into the implications of our model for the less-explored case of eccentric orbits, highlighting the key role of the geometric correction factor in shaping the accretion process. We compare our predictions with numerical simulations, finding good agreement for a wide range of parameters. Applications to the symbiotic star R Aqr and the X-ray binary LS 5039 are presented. This improved model offers a more accurate description of wind accretion in binary systems, with implications for stellar evolution, population synthesis, and observational data interpretation.

**Keywords:** Binary Stars (154); Stellar accretion (1578); Stellar Winds (1636); High mass X-ray binary stars (733); Symbiotic binary stars (1674)

## 1. INTRODUCTION

Mass transfer in binary systems is crucial to understand accretion onto compact objects and stellar evolution. This process is key in a wide range of scenarios, powering phenomena such as cataclysmic and symbiotic binaries, novae, supernovae, and X-ray binaries (Frank et al. 2002). The Bondi-Hoyle-Lyttleton (BHL) accretion model, developed initially by Hoyle & Lyttleton (1939) and later refined by Bondi & Hoyle (1944) and Bondi (1952), constitutes a foundational framework for analyzing this mass transfer by providing a theoretical estimate of the rate at which a compact object captures material from a wind.

The BHL model's appeal lies in its straightforward approach, offering a clear basis for understanding wind accretion. Its relative simplicity makes it a valuable tool, serving as a starting point for more complex accretion scenarios (Romero & Vila 2014). However, the model's assumptions, such as a point-like accretor and a uniform

wind, oversimplify the complexities of real astrophysical systems. Factors like the nonuniform nature of stellar winds, interactions with radiation fields, and the influence of magnetic fields necessitate modifications and extensions to the BHL formalism (see review by Edgar 2004).

The BHL model has been applied to a wide range of binary systems, showcasing its versatility. In symbiotic binaries, where a white dwarf (WD) accretes from the wind of a late-type giant companion, the BHL model provides insights into the accretion rates that can trigger outbursts and influence stellar evolution (de Val-Borro et al. 2009; Saladino et al. 2018). On the other hand, in high-mass X-ray binaries (HMXBs), where a compact object accretes from the wind of a massive star, the BHL model provides a basic understanding of the accretion process and the resulting X-ray emission (Davidson & Ostriker 1973; Martínez-Núñez et al. 2017; Negueruela 2010; Reig et al. 2003), as well as the estimation of the system parameters and other observational features (Eadie et al. 1975). In addition, it has been also used as benchmark for the more complex common envelope scenario (e.g., Chen et al. 2018; López-Cámara et al. 2022; El-Badry et al. 2023).

However, the BHL model faces limitations when the wind velocity  $v_w$  is comparable to or less than the orbital velocity  $v_o$  of the accretor (Boffin 2015; Hansen et al. 2016). This is particularly relevant for symbiotic systems for which simulations predict a flattening of the mass accretion efficiency when  $v_w \ll v_o$  (Nagae et al. 2004; Saladino et al. 2019), while the commonly used analytical formula for the BHL accretion rate leads to nonphysical mass capture efficiencies exceeding unity. For instance, observations of the symbiotic system *o* Ceti predict a mass accretion onto its WD component of  $10^{-10} M_\odot \text{ yr}^{-1}$ , a couple of orders of magnitude below that predicted by the classic BHL model (Sokoloski & Bildsten 2010). Such discrepancies highlight the need for refinements to the BHL model, especially in scenarios with low wind-to-orbital velocity ratios.

Several authors have proposed modifications to the BHL formalism to address these limitations, for example, incorporating arbitrary efficiency factors or cut-off values (see e.g., Nagae et al. 2004; Saladino et al. 2019; Malfait et al. 2024). However, these modifications often have limited applicability. In this article, we revisit the BHL model and introduce a simple geometric correction factor that yields improved agreement between theoretical predictions and numerical simulations across a wider range of wind-to-orbital velocity ratios.

Importantly, our modified model naturally reproduces the flattening of the mass accretion efficiency observed in simulations when  $v_w \ll v_o$ , without the need for arbitrary adjustments. Furthermore, we extend our analysis to binary systems with eccentric orbits, aiming to improve the accuracy of BHL accretion rate predictions in these more intricate systems, which are crucial for understanding the long-term evolution and observational signatures of a variety of astrophysical phenomena.

This paper is organized as follows. Section 2 describes the modified BHL approach, detailing the geometric correction factor and the resulting mass accretion efficiency. Section 3 presents the results for both circular and elliptical orbits, including comparisons with numerical simulations. Section 4 discusses the implications of these results, particularly for symbiotic stars and HMXBs, and addresses the limitations and potential refinements of the model. Finally, Section 5 summarizes the key findings.

## 2. ANALYTICAL MODEL

We consider a binary system composed of a donor star  $m_1$  and an accreting companion  $m_2$ . The primary star loses mass via a stationary stellar wind, and the secondary accretes material from this wind as it goes around its trajectory (see Fig 1).

Given the orbital parameters, semi-major axis  $a$  and eccentricity  $e$ , the accretor's trajectory around the primary

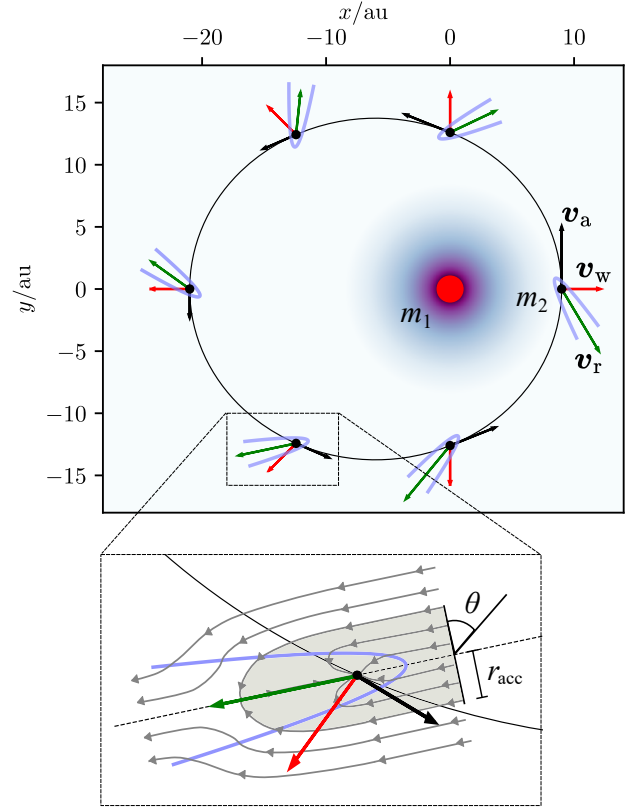


**Figure 1.** Illustration of BHL accretion in a binary system, highlighting the geometric correction factor. The binary system has  $m_1 = 3 M_\odot$ ,  $m_2 = 1 M_\odot$ ,  $a = 15 \text{ au}$ , and  $e = 0.4$ , with a constant radial wind velocity of  $20 \text{ km s}^{-1}$ . The accretor's elliptical trajectory around the primary is shown, with velocity vectors for the accretor ( $v_a$ , black arrow), the primary's stellar wind ( $v_w$ , red arrow), and their relative velocity ( $v_r$ , green arrow). Parabolic shapes qualitatively indicate the expected location of the accretion wake at each position. *Inset:* Accretion flow streamlines around the secondary. The shaded area represents the fraction of the incoming wind accreted by the secondary, visualized as being within an accretion cylinder of radius  $r_{\text{acc}}$ . The angle  $\theta$  between  $v_w$  and  $v_r$  highlights the need to account for a projection factor when applying the BHL model to binary systems.

is described by

$$r(\varphi) = \frac{a(1 - e^2)}{1 + e \cos \varphi}, \quad (1)$$

$$\mathbf{v}_a = \frac{v_o}{\sqrt{1 - e^2}} [(e \sin \varphi) \hat{r} + (1 + e \cos \varphi) \hat{\varphi}], \quad (2)$$

where  $v_o = \sqrt{G(m_1 + m_2)/a}$  is the mean orbital velocity of the accretor,  $\varphi$  is the true anomaly, and  $\hat{r}$  and  $\hat{\varphi}$  are the unit vectors in the radial and azimuthal directions, respectively.

The stellar wind of the donor can be characterized by its mass-loss rate  $\dot{M}_w$ . Assuming that the stellar wind is stationary and isotropic, at any distance  $r$  from the primary,

it satisfies

$$\dot{M}_w = 4\pi r^2 v_w \rho_w, \quad (3)$$

where  $v_w$  is the wind velocity and  $\rho_w$  is the wind density at radius  $r$ . We adopt a  $\beta$  velocity law for the wind (Lamers & Cassinelli 1999)

$$v_w(r) = v_\infty \left(1 - \frac{R}{r}\right)^\beta \hat{r}, \quad (4)$$

where  $v_\infty$  is the terminal wind speed,  $R$  is the wind launching radius, and  $\beta$  is an exponent determining how quickly the terminal speed is reached.

The relative velocity between the accretor and the stellar wind is

$$\mathbf{v}_r = \mathbf{v}_w - \mathbf{v}_a, \quad (5)$$

with its magnitude given by

$$v_r = \sqrt{v_w^2 + v_a^2 - 2v_w v_a^r}, \quad (6)$$

where

$$v_a = v_o \sqrt{\frac{2a}{r} - 1} \quad (7)$$

is the magnitude of the accretor's velocity and

$$v_a^r = \frac{e v_o \sin \varphi}{\sqrt{1 - e^2}}, \quad (8)$$

is its radial component.

According to the BHL model, a point mass accretes from a wind with which it has a relative velocity  $v_r$  at a rate

$$\dot{M}_{\text{BHL}} = \pi r_{\text{acc}}^2 \rho_w v_r, \quad (9)$$

where

$$r_{\text{acc}} = \frac{2Gm_2}{v_r^2}, \quad (10)$$

is the radius of the accretion cylinder.

To generalize Equation (9) for accreting binaries in elliptical orbits, we must account for the varying orientation of the accretion cylinder relative to the wind (see inset in Figure 1). Since the wind is assumed to be uniformly spread over a sphere ( $4\pi r^2$ ), the accretion cylinder's cross-sectional area will intercept a different fraction of the wind depending on its instantaneous position in the orbit. Given that the relative velocity  $\mathbf{v}_r$  is perpendicular to this cross-section, we can determine the angle  $\theta$  between the wind velocity  $\mathbf{v}_w$  and the accretion cylinder's area as

$$\cos \theta = \frac{\mathbf{v}_r \cdot \mathbf{v}_w}{v_r v_w} = \frac{v_w - v_a^r}{v_r}. \quad (11)$$

Taking this geometric effect into account, we can express the mass accretion efficiency as

$$\eta = \frac{\dot{M}_{\text{BHL}}}{\dot{M}_w} \cos \theta = \frac{1}{4} \left| 1 - \frac{v_a^r}{v_w} \right| \left( \frac{r_{\text{acc}}}{r} \right)^2. \quad (12)$$

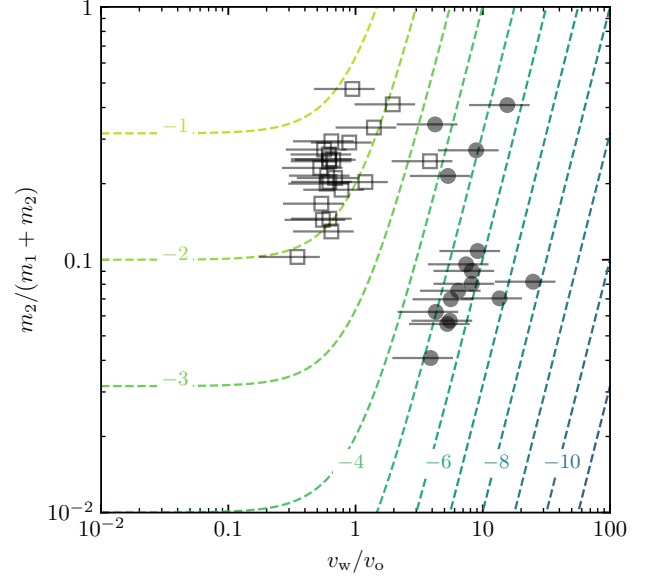


**Figure 2.** Mass accretion efficiency  $\eta$  contour plot for circular orbits (Equation 14) as a function of the dimensionless wind velocity  $w = v_w/v_o$  and mass ratio  $q = m_2/(m_1 + m_2)$ . Dashed lines indicate contours of constant  $\log_{10}(\eta)$ . The parameter space occupied by observed high-mass X-ray binaries (HMXB) is represented by filled bullets, assuming a wind velocity range of 1000–3000 km s<sup>-1</sup> with an average of 2000 km s<sup>-1</sup>. Empty squares represent symbiotic systems, where a wind velocity range of 10–30 km s<sup>-1</sup> with an average of 20 km s<sup>-1</sup> has been assumed. See Appendix A for further details on the data.

In contrast, if we neglect the geometric projection factor (Equation 11), the mass accretion efficiency reduces to the classic formulation

$$\eta_{\text{BHL}} = \frac{1}{4} \frac{v_r}{v_w} \left( \frac{r_{\text{acc}}}{r} \right)^2, \quad (13)$$

which has been widely employed in the literature (see, e.g., Boffin & Jorissen 1988; Theuns et al. 1996; Nagae et al. 2004; Liu et al. 2017; Saladino et al. 2019; El Mellah et al. 2019; ?).

It is worth noting that somewhat similar expressions for the mass accretion efficiency described by Equation (12) have been previously presented in the literature, albeit with important differences and less clear derivations (Reig et al. 2003; Bozzo et al. 2021). However, our formulation provides a more rigorous and transparent derivation based on geometric considerations, leading to a clearer physical interpretation and broader applicability.

### 3. MODEL PREDICTIONS

#### 3.1. Circular orbits

**Table 1.** Comparison between the mass accretion efficiency ( $\eta$ ) of the modified BHL approach presented in this paper, the classic BHL model ( $\eta_{\text{BHL}}$ ), and prediction of the mass accretion efficiency obtained from simulations ( $\eta_{\text{sim}}$ ). For the eccentric cases, the mass accretion estimates correspond to averaged values.

Reference	$e$	$m_1$ [ $M_\odot$ ]	$m_2$ [ $M_\odot$ ]	$q$	$v_o$ [ $\text{km s}^{-1}$ ]	$v_w$ [ $\text{km s}^{-1}$ ]	$w$	$\eta_{\text{sim}}$ [%]	$\eta$ [%]	$\eta_{\text{BHL}}$ [%]
Theuns et al. (1996)	0.0	3	1.5	0.33	36.5	15	0.42	8	8.1	21.4
de Val-Borro et al. (2009)	0.0	1.2	0.6	0.33	10.00	6	0.60	6	6	11.6
Huarte-Espinosa et al. (2013)	0.0	1.5	1.0	0.40	14.90	10	0.67	8.5	7.6	13.6
	0.0	1.5	1.0	0.40	12.16	10	0.67	5	5.7	9.0
	0.0	1.5	1.0	0.40	10.53	10	0.67	3	4.4	6.4
Chen et al. (2020)	0.0	1.02	0.51	0.33	14.40	15.8	1.10	1.8	2.3	5.3
Lee et al. (2022)	0.0	1.5	0.6	0.29	30.50	13.7	0.45	20.8±5.6	5.7	13.8
	0.0	1.5	0.6	0.29	30.50	15.1	0.50	11.1±3.8	5.3	11.9
	0.0	1.5	0.6	0.29	30.50	16.7	0.55	12.4±3.6	4.8	10.1
	0.0	1.5	0.6	0.29	30.50	18.5	0.61	4.8±1.3	4.4	8.4
	0.0	1.5	0.6	0.29	30.50	20.4	0.67	3.6±2.2	3.9	7.0
	0.0	1.5	0.6	0.29	30.50	21.8	0.71	4.3±1.9	3.6	6.2
	0.0	1.5	0.6	0.29	30.50	23.9	0.74	2.2±1.9	3.1	5.1
Malfait et al. (2024)	0.0	1.5	1.0	0.40	19.23	12.7	0.66	12.5	7.8	14.1
	0.0	1.5	1.0	0.40	19.23	15.0	0.78	9.9	6.2	10.1
	0.0	1.5	1.0	0.40	19.23	22.8	1.19	4.0	2.8	3.6
Saladino & Pols (2019)	0.2	1.2	0.6	0.33	17.90	15.1	0.84	7.1	8.1	22.6
	0.4	1.2	0.6	0.33	15.51	15.1	0.97	4.6	6.0	14.5
	0.6	1.2	0.6	0.33	12.65	15.1	1.19	2.6	3.9	8.5
	0.8	1.2	0.6	0.33	8.95	15.1	1.69	1.0	1.8	3.7
Malfait et al. (2024)	0.5	1.5	1.0	0.40	19.23	12.7	0.66	20.6	11.3	26.6
	0.5	1.5	1.0	0.40	19.23	15.0	0.78	12.3	9.5	19.6
	0.5	1.5	1.0	0.40	19.23	22.8	1.19	4.3	4.4	6.7

For circular orbits, we can simplify the mass accretion efficiency expression given by Equation (12) as

$$\eta = \left[ \frac{Gm_2}{a(v_o^2 + v_w^2)} \right]^2 = \left( \frac{q}{1 + w^2} \right)^2, \quad (14)$$

where we have introduced the dimensionless ratios

$$q = \frac{m_2}{m_1 + m_2}, \quad (15)$$

$$w = \frac{v_w}{v_o}. \quad (16)$$

This result is consistent with that of Hirai & Mandel (2021), who employed a different derivation. Interestingly, in the case of circular orbits, the expressions derived by Reig et al. (2003) and Bozzo et al. (2021), despite their differing approaches, also reduce to Equation (14), yielding the same result as our model.

The concise formulation in Equation (14) underscores that, for circular orbits, the mass accretion efficiency is entirely determined by the ratios  $q$  and  $w$ . We illustrate this dependence in Figure 2, plotting  $\eta$  as a function of  $q$  and  $w$ . To provide context, we also indicate the parameter space occupied by representative symbiotic systems and HMXBs (see Appendix A for the complete list of objects). It is noteworthy that the four highest bullet points in the figure correspond to HMXB known to host black holes.

From Equation (14), we can derive the asymptotic behavior of the mass accretion efficiency  $\eta$  in two limiting regimes.

When the wind speed significantly dominates the orbital velocity ( $w \gg 1$ ), the efficiency scales as

$$\eta \simeq \frac{q^2}{w^4}, \quad (17)$$

which recovers the behavior of  $\eta_{\text{BHL}}$  (Equation 13) in this regime. Conversely, when the orbital velocity is much larger than the wind speed ( $w \ll 1$ ), the efficiency becomes independent of  $w$  and approaches a constant value

$$\eta \simeq q^2. \quad (18)$$

A key advantage of our formulation in Equation (14) is that it guarantees physically plausible mass accretion efficiencies ( $\eta \leq 1$ ) for any combination of values  $q$  and  $w$ . This is especially relevant when the orbital velocity exceeds the wind speed ( $w \ll 1$ ), a regime where the classic BHL model leads to nonphysical predictions, as discussed in Section 1.

To assess the accuracy of our modified BHL model, we selected influential works from the literature that cover a range of relevant parameters and physical conditions. These works, which employ different numerical methods and vary in the way they model the primary's wind, provide numerical simulations of mass accretion efficiency ( $\eta_{\text{sim}}$ ), allowing us to compare them with our predictions for  $\eta$  (Equation 14) and the classic BHL efficiency  $\eta_{\text{BHL}}$  (Equation 13). A summary of this comparison is shown in Table 1. We note that, in general, our modified analytical estimation of  $\eta$  agrees very well with  $\eta_{\text{sim}}$  from different works.

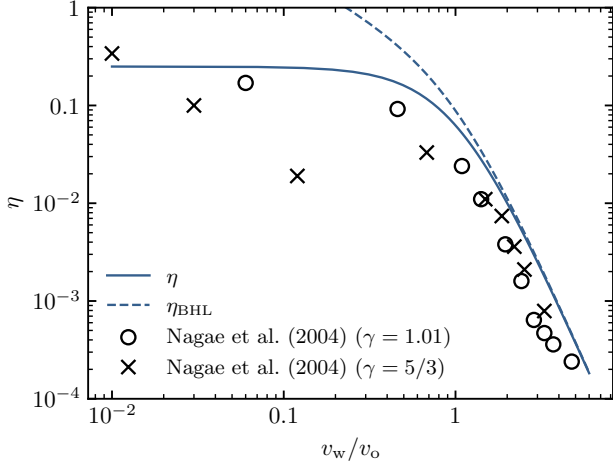


**Figure 3.** Comparison between the mass accretion efficiency predicted by the modified BHL proposed in this work ( $\eta$  – solid line) versus that of the classic model ( $\eta_{\text{BHL}}$  – dashed line). The calculations have been computed for a binary system with  $q = 0.5$ . The symbols show the results from numerical simulation from Nagae et al. (2004).

We note that the largest discrepancies between our model and the simulations are found in the studies by Lee et al. (2022) and Malfait et al. (2024), where the wind is still being accelerated within the spatial domain of interest. This ongoing acceleration complicates the comparison, as it becomes ambiguous to choose an appropriate value for the wind velocity in our model, which ideally should correspond to the wind velocity at the location of the secondary. We will explore the possible implications of this ambiguity and other factors contributing to the discrepancies in Section 4.

Having established the overall agreement, we present now a closer comparison with specific numerical simulations. In Figure 3, we use data from Nagae et al. (2004), who presented a series of simulations for both adiabatic ( $\gamma = 5/3$ ) and isothermal ( $\gamma = 1.01$ ) cases with a mass ratio of  $q = 0.5$ . The figure compares the predictions of  $\eta$  and  $\eta_{\text{BHL}}$  for a circular orbit as a function of  $w$ . As can be seen, incorporating the geometric factor into the BHL approximation significantly improves the agreement with the numerical results. Our model accurately captures the flattening of the accretion efficiency observed in the simulations for low wind-to-orbital velocity ratios. The figure also demonstrates the two asymptotic behaviors of  $\eta$  established by Equations (17) and (18), and highlights the inadequacy of the classic BHL approach ( $\eta_{\text{BHL}} > 1$ ) for low  $w$ .

More recently, Saladino et al. (2019) presented a series of SPH simulations of accreting binaries covering a wide range of parameters (see their table 3). As expected, they found that for models with large  $w$ , the resulting efficiency closely matches the classic BHL prediction ( $\eta_{\text{sim}} \approx \eta_{\text{BHL}}$ ). However, for low  $w$ , they observed that  $\eta_{\text{sim}}$  never exceeds

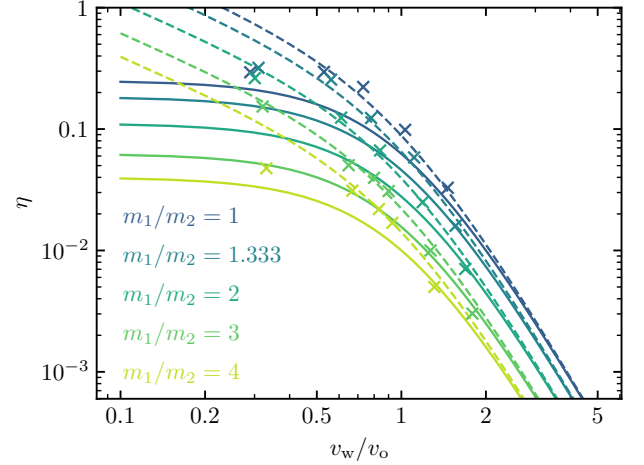


**Figure 4.** Mass accretion efficiency  $\eta$  predicted by our modified BHL model calculated for different mass ratios. The (cross) symbols represent the results obtained from the numerical simulations presented in Saladino et al. (2019). The dashed lines are the predictions of the classic BHL approximation ( $\eta_{\text{BHL}}$ ).

30%. To incorporate these findings into a binary population synthesis code, Saladino et al. (2019) fitted their low- $w$  ( $w < 1$ ) data with constant values.

Figure 4 compares our model’s predictions with the results from Saladino et al. (2019). Remarkably, our modified BHL model naturally predicts the flattening of the mass accretion efficiency observed in the simulations for  $w < 1$ , without the need for any fitting procedures. While the simulations show a similar trend to our model, slight differences are apparent, likely due to the inclusion of cooling physics in the simulations, which our model does not incorporate.

### 3.2. Elliptic orbits

For a general eccentric case, the mass accretion efficiency  $\eta$  is given by Equation (12). We can rewrite this expression in terms of dimensionless quantities as

$$\eta = q^2 \left| 1 - \frac{e \sin \varphi}{w(\varphi) \sqrt{1 - e^2}} \right| \frac{(1 + e \cos \varphi)^2}{1 - e^2} \times \left[ w(\varphi)^2 - 1 + 2 \left( \frac{1 + e \cos \varphi - w(\varphi) e \sin \varphi}{\sqrt{1 - e^2}} \right) \right]^{-2}, \quad (19)$$

with  $q$  is defined in Equation (15) and  $w(\varphi)$  is now a function of the orbital phase that, according to Equation (4), we can write as

$$w(\varphi) = w_\infty \left[ 1 - \frac{R(1 + e \cos \varphi)}{a(1 - e^2)} \right]^\beta, \quad (20)$$

with  $w_\infty = v_\infty/v_o$ .

From Equation (19), we observe that  $\eta$  varies periodically throughout the orbit. To characterize the overall accretion

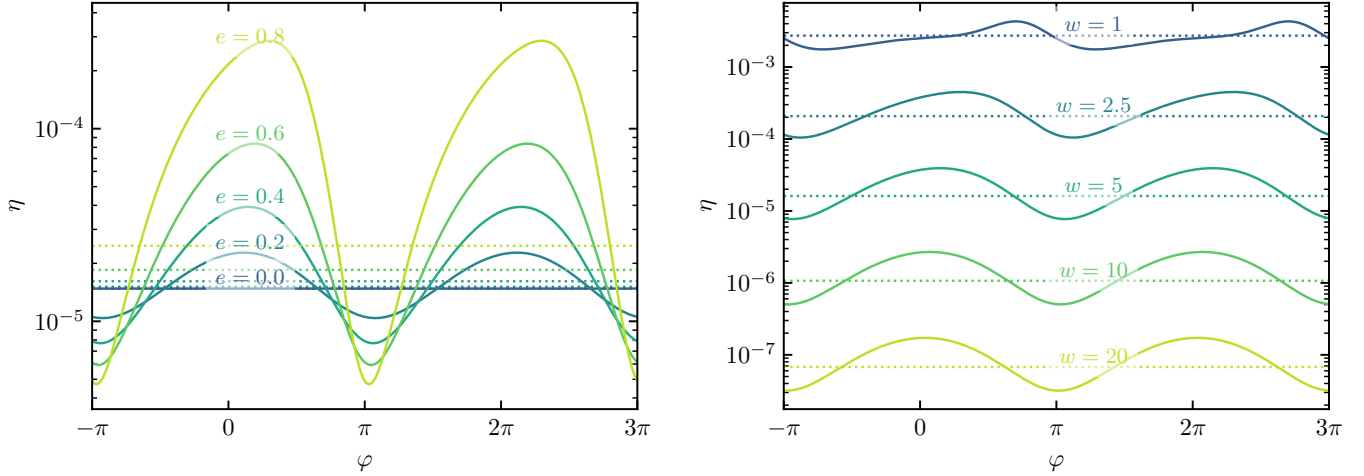


**Figure 5.** Mass accretion efficiency  $\eta$  for elliptical orbits with  $q = 0.1$  as a function of orbital phase. *Left:* Models with varying eccentricity  $e$  and a fixed wind-to-orbital velocity ratio of  $w = 5$ . *Right:* Models with varying  $w$  and a fixed eccentricity of  $e = 0.4$ . The corresponding parameter values for each curve are labeled in the respective panels. The average mass accretion efficiency  $\eta_{\text{avg}}$  is indicated by dotted horizontal lines for each model.

behavior, we determine the average mass accretion efficiency  $\eta_{\text{avg}}$  by integrating  $\eta$  over a full orbital period  $T$  as

$$\begin{aligned} \eta_{\text{avg}} &= \frac{1}{T} \int_0^T \eta dt = \frac{1}{T} \int_0^{2\pi} \eta \frac{r^2}{h} d\varphi \\ &= \frac{(1-e^2)^{3/2}}{2\pi} \int_0^{2\pi} \frac{\eta}{(1+e \cos \varphi)^2} d\varphi. \end{aligned} \quad (21)$$

### 3.3. Representative parameters for high-mass X-ray binaries

Figure 5 presents examples of eccentric models with a fixed mass ratio of  $q = 0.1$ , where we have also considered that the wind has already reached its asymptotic velocity for the entire spatial domain (that is,  $\beta = 0$ ). The figure is divided into two panels: the left panel explores the effect of varying the eccentricity  $e$  while keeping the wind-to-orbital velocity ratio fixed  $w = 5$ , and the right panel examines the influence of varying  $w$  for a fixed eccentricity of  $e = 0.4$ . These values are representative of typical HMXB systems (see Figure 2 and Appendix A).

From both panels, we can observe that the resulting curves for the mass accretion efficiency are more symmetric and sinusoidal-like for cases with small  $e$  or large  $w$ . In these cases, the maxima and minima of the curves correspond quite closely to the positions of periastron and apastron, respectively. However, as  $e$  increases and  $w$  decreases, the curves become increasingly asymmetric. The maximum shifts notably towards the minimum, resulting in a shallower rise towards periastron and a steeper decline towards apastron, as seen in the curves for  $e = 0.8$  and  $w = 1$  in the left and right panels, respectively. This asymmetry arises from the complex interplay between the accretor's velocity, the wind velocity, and the varying distance between the stars along the eccentric orbit.

Focusing now on the left panel of Figure 5, we see that, as the eccentricity increases, the peak-to-valley ratio of the curves also increases, spanning almost two orders of magnitude for the  $e = 0.8$  model. The averaged mass accretion efficiency  $\eta_{\text{avg}}$ , illustrated with dotted horizontal lines, also increases with  $e$ . This trend arises because, even though the relative velocity is larger close to periastron and the accretor spends less time there, the mass accretion is more efficient due to the enhanced wind density in this region. This enhanced density outweighs the effects of increased velocity and reduced time of passage, leading to a net increase in the average accretion efficiency with eccentricity.

The right panel of Figure 5 shows the variations in mass accretion efficiency for different values of  $w$ , with the eccentricity fixed at  $e = 0.4$ . Similarly to Equation (17), as  $w$  increases, the mass accretion becomes less efficient. For instance, a model with  $w = 20$  has an average mass accretion efficiency of  $\eta_{\text{avg}} \approx 7 \times 10^{-8}$ , while a model with  $w = 2.5$  results in  $\eta_{\text{avg}} \approx 3 \times 10^{-4}$ .

In Figure 6, we delve into the impact of different wind acceleration profiles on the mass accretion efficiency. To isolate this effect, we fix the mass ratio  $q$ , eccentricity  $e$ , and wind-to-orbital velocity ratio  $w_\infty = v_\infty/v_0$  to representative values, and explore the influence of the wind acceleration parameter  $\beta$  which ranges from 0 (instantaneous acceleration) to 2 (gradual acceleration). As the figure demonstrates, while the specific value of  $\beta$  does not significantly affect the average mass accretion efficiency, it can substantially alter the shape of the efficiency curve. A smoother wind acceleration ( $\beta$  closer to 2) leads to the emergence of two additional extremal points: a local maximum and a local minimum. Moreover, as  $\beta$  increases, the ratio between the global maximum and minimum also increases, and both extrema appear to shift closer to apastron,

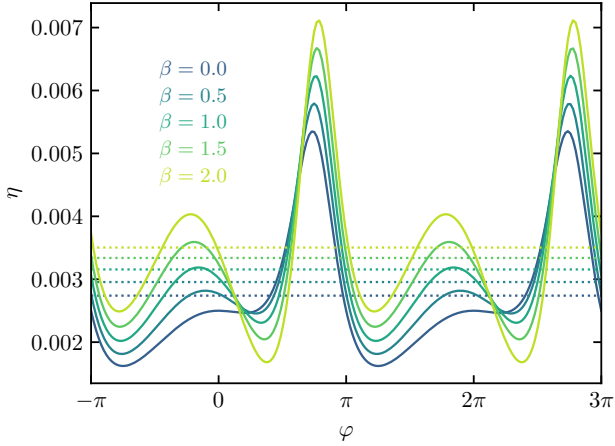


**Figure 6.** Mass accretion efficiency  $\eta$  for elliptical cases with  $q = 0.1$ ,  $e = 0.5$ , and  $w_\infty = 1$ , showcasing the influence of different wind acceleration profiles. The wind acceleration is modeled by Equation (20) with varying values of  $\beta = 0, 0.5, 1, 1.5, 2$ , and a fixed wind launching radius of  $R = 0.1 a$ .

resulting in an abrupt rise and drop in the mass accretion efficiency at that orbital position.

### 3.4. Representative parameters for symbiotic systems

Figure 7 presents calculations for elliptical models with  $q = 0.25$ ,  $\beta = 0$ , and varying  $w$  values, chosen to be representative of typical symbiotic systems (see Figure 2 and Appendix A). The left panel focuses on models with an eccentricity of  $e = 0.08$ , which is the median value obtained from all confirmed galactic symbiotic systems in the *New Online Database of Symbiotic Variables* with available information (Merc et al. 2019). The right panel, in contrast, explores a higher eccentricity of  $e = 0.4$  to illustrate the impact of more eccentric orbits on the accretion process.

As seen in the left panel, the average mass accretion efficiency  $\eta_{\text{avg}}$  increases as  $w$  decreases, as predicted by the classical BHL model. Interestingly, even with the relatively modest eccentricity of  $e = 0.08$ , the range of mass accretion efficiency values increases significantly as  $w$  decreases, as evidenced by the growing ratio between the maximum and minimum values. This highlights the impact of even small eccentricities on the accretion process, particularly for slower winds.

Furthermore, the figure reveals that both the minimum and maximum efficiency shift to smaller orbital phases  $\varphi$  as  $w$  increases. For instance, with  $w = 0.1$ , the maximum is reached after apastron at  $\varphi \simeq 4.4$ , whereas for  $w = 0.8$ , it occurs before apastron at  $\varphi \simeq 2.2$ .

On the right panel of Figure 7, where we consider a higher eccentricity of  $e = 0.4$ , we observe similar trends to those in the left panel. However, a new qualitative feature emerges: for sufficiently large values of  $w$ , the mass accretion efficiency completely vanishes at two points in the orbital phase. This intriguing behavior arises from the

geometric projection factor in Equation (12), which becomes zero whenever the wind velocity ( $v_w$ ) equals the radial component of the accretor's velocity ( $v_a^r$ ). At these specific points, the wind direction is instantaneously perpendicular to the accretion cylinder, resulting in no material being captured.

Using Equation (19), the general condition for the vanishing of mass accretion efficiency can be expressed as

$$\frac{e \sin \varphi}{\sqrt{1 - e^2}} = \frac{v_\infty}{v_o} \left[ 1 - \frac{R(1 + e \cos \varphi)}{a(1 - e^2)} \right]^\beta. \quad (22)$$

For an arbitrary value of  $\beta$ , this equation requires numerical methods to find solutions. However, we can derive analytical solutions for the specific case where the wind has already reached its terminal velocity  $v_w = v_\infty$  throughout the relevant domain ( $\beta = 0$ ). In this scenario, the mass accretion efficiency vanishes if

$$w \leq \frac{e}{\sqrt{1 - e^2}}, \quad (23)$$

which occurs at the following two orbital phases

$$\varphi_1 = \arcsin(w\sqrt{1 - e^2}/e), \quad (24)$$

$$\varphi_2 = \pi - \varphi_1. \quad (25)$$

These two points first appear at  $\varphi_1 = \varphi_2 = \pi/2$  when  $w = e/\sqrt{1 - e^2}$ . As  $w$  decreases below this threshold ( $w < e/\sqrt{1 - e^2}$ ), the points split symmetrically, moving away from  $\pi/2$  and always satisfying  $0 < \varphi_1 < \varphi_2 < \pi$ , as seen in the right panel of Figure 7). This behavior indicates that these points of vanishing accretion efficiency emerge exclusively during the accretor's motion from periastron to apastron.

While a complete cancellation of the accretion efficiency is unlikely under more realistic astrophysical conditions with clumps, shocks, and velocity variations in stellar winds, our model suggests that, under appropriate circumstances with sufficiently high eccentricities and low wind velocities, one could expect to observe orbital phases with a sharp decline in accretion. This prediction offers a potentially testable observational signature of our modified BHL model.

## 4. DISCUSSION

Understanding the accretion process is fundamental to advancing our knowledge of the evolution of interacting binaries, as it significantly influences the evolutionary path of both stars. Accretion also directly affects the observable properties of these systems, such as the luminosity of symbiotic stars and HMXBs, which can be directly compared with optical and X-ray observations (see for example Pujol et al. 2023; Toalá et al. 2024; Zamanov et al. 2024).

However, as discussed in Section 1, the classic BHL model faces limitations when the wind velocity is less than the orbital velocity ( $w < 1$ ), a regime relevant to most symbiotic systems. In this regime, the classic BHL model

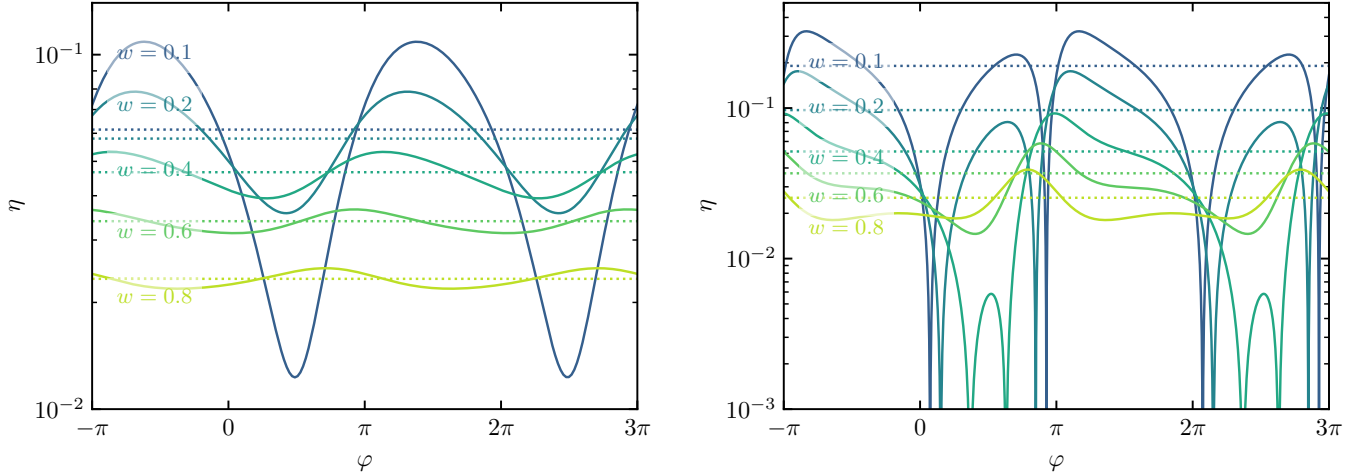


**Figure 7.** Mass accretion efficiency  $\eta$  for elliptical cases with  $q = 0.25$  as a function of orbital phase for different  $w$  values as labeled in the figure. The left and right panels show the results for  $e = 0.08$  and  $e = 0.40$ , respectively. The averaged mass accretion efficiency ( $\eta_{\text{avg}}$ ) is shown with dotted lines for all models.

(Equation 13) can predict nonphysical accretion efficiencies exceeding unity, an inadequacy corroborated by numerical studies (e.g., Nagae et al. 2004; Saladino et al. 2019; El Mellah et al. 2019). This has led to the prevailing view that the classic BHL model is only applicable in the high wind-to-orbital velocity regime ( $w > 1$ ; see, e.g., Boffin 2015; Hansen et al. 2016).

In this work, we have addressed this limitation by incorporating a geometric projection factor within the classic BHL framework, extending its applicability to arbitrarily small values of  $w$ . This modification, derived from simple geometric considerations, provides a unified and physically motivated description of wind accretion, accurately capturing the accretion dynamics across a wide range of wind-to-orbital velocity ratios.

For circular orbits, our modified model (Equation 14) predicts that the accretion efficiency  $\eta$  depends solely on the dimensionless ratios  $q$  and  $w$ , always guaranteeing physically plausible values  $\eta \leq 1$ . It recovers the classic BHL scaling  $\eta = q^2/w^4$  for  $w \gg 1$  (Equation 17) and predicts a constant efficiency  $\eta = q^2$  for  $w \ll 1$  (Equation 18), consistent with numerical simulations.

This improved accuracy has significant implications for modeling binary systems. Previous studies, such as those by Vos et al. (2015) and Abate et al. (2015), relied on accretion prescriptions tailored to the  $w \gg 1$  regime. By incorporating our modified BHL formalism, which accurately captures the accretion efficiency across the full range of  $w$ , future models will be able to achieve more precise predictions of binary system evolution, including the circularization process of elliptical orbits (e.g., Bonačić Marinović et al. 2008; Saladino & Pols 2019; Misra et al. 2023). Furthermore, our approach offers a simplification compared to the more intricate prescriptions of Saladino et al. (2019), while maintaining broad applicability.

#### 4.1. Applications: two representative examples

To illustrate the versatility of our modified BHL model, we now apply it to two distinct types of accreting binary systems: symbiotic stars and HMXBs. As shown in Figure 2, these systems occupy different regions of the parameter space. HMXBs typically reside in the high wind-to-orbital velocity ratio regime ( $w > 1$ ), where the classic BHL approximation remains valid. In contrast, symbiotic stars are generally found in the  $w \lesssim 1$  regime, where the classic BHL model overestimates the accretion efficiency and the geometric correction becomes crucial. Furthermore, symbiotic systems exhibit higher mass accretion efficiencies ( $\eta = 0.01 - 0.1$ ) compared to HMXBs ( $\eta = 10^{-8} - 10^{-4}$ ), indicating a more efficient capture of material from their mass-losing companions.

##### 4.1.1. *R Aquarii*: a symbiotic system

Figure 8 presents our model's predictions for the evolution of the mass accretion efficiency in the symbiotic system R Aqr, one of the best-characterized systems of this type. R Aqr has an orbital period of 42 years, with stellar component masses of  $m_1 = 1.0 M_\odot$  and  $m_2 = 0.7 M_\odot$ , and an eccentricity of  $e = 0.45$  (see Alcolea et al. 2023, and references therein). Adopting a mass-loss rate of  $\dot{M}_w = 10^{-7} M_\odot \text{ yr}^{-1}$  (Michalitsianos et al. 1980; Spiegel et al. 1983) and wind velocities of 25, 30, and 35  $\text{km s}^{-1}$ , our model predicts average mass accretion efficiencies of  $7 \times 10^{-4}$ ,  $4 \times 10^{-4}$ , and  $2 \times 10^{-4}$ , respectively. These efficiencies correspond to mass accretion rates onto the white dwarf component of  $7.4 \times 10^{-10}$ ,  $4.0 \times 10^{-10}$ , and  $2.4 \times 10^{-10} M_\odot \text{ yr}^{-1}$ , aligning well with observational estimates (Vasquez-Torres, Toalá, et al. submitted).

##### 4.1.2. *LS 5039*: a high-mass X-ray binary



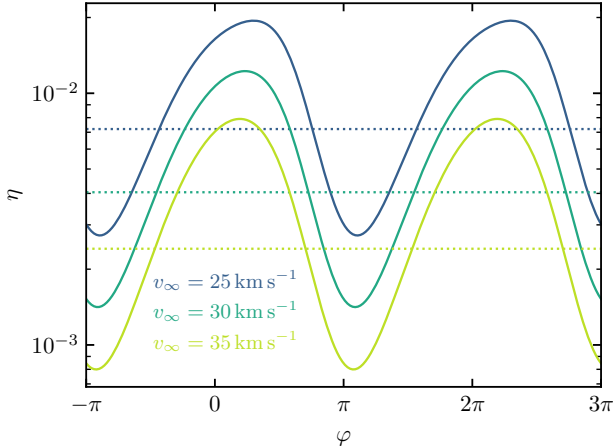


**Figure 8.** Prediction of the mass accretion efficiency  $\eta$  for the symbiotic system R Aqr. Results are shown for three different terminal wind velocities, as labeled.

We now turn our attention to LS 5039, a HMXB system whose compact accretor has been the subject of much debate (Casares et al. 2005; Yoneda et al. 2020; Volkov et al. 2021; Makishima et al. 2023). Multi-epoch X-ray observations have revealed an average flux of  $F_X \lesssim 10^{-11}$  erg cm $^{-2}$  s $^{-1}$  in the 1–10 keV band (Zabalza et al. 2008; Takahashi et al. 2009), which, at a distance of 2.5 kpc, translates to an average X-ray luminosity of  $L_{X,\text{avg}} \approx 7 \times 10^{33}$  erg s $^{-1}$ .

Detailed orbital analysis of LS 5039 suggests an eccentricity of  $e = 0.35$ , a period of  $T = 3.9$  days, and a massive O-type companion star with a mass of  $m_1 = 22.9 M_\odot$  and a radius of  $9.3 R_\odot$  (Casares et al. 2005). The nature of the compact object remains uncertain, with possibilities including a black hole (BH) of mass  $m_{\text{BH}} = 3.7 M_\odot$  or a neutron star (NS) of mass  $m_{\text{NS}} = 1.4 M_\odot$  and radius  $R_{\text{NS}} = 10$  km (Casares et al. 2005).

To investigate the nature of the accretor, we apply our modified BHL model, adopting a primary’s wind with terminal velocity of  $2440$  km s $^{-1}$ , a mass loss rate of  $\dot{M}_w$   $1\text{--}2 \times 10^{-7}$ , and  $\beta = 0.8$  (Casares et al. 2005; Dubus et al. 2015; Reig et al. 2003; Kissmann et al. 2023). We estimate the resulting accretion luminosity  $L_X$  assuming that the accreted material forms a thin accretion disk around the compact object. We use the standard expression for this process (Shakura & Sunyaev 1973):

$$L_X = \frac{1}{2} \frac{Gm_2}{r_{\text{in}}} \dot{M}_{\text{acc}}, \quad (26)$$

where  $\dot{M}_{\text{acc}} = \eta \dot{M}_w$ ,  $m_2$  is the mass of the accreting object, and  $r_{\text{in}}$  is the inner radius of the accretion disk. For a weakly magnetized NS, we can take  $r_{\text{in}} = R_{\text{NS}} = 10$  km, while for a non-rotating BH, we take the radius of the innermost stable circular orbit:  $r_{\text{in}} = 6Gm_{\text{BH}}/c^2 \simeq 32.9$  km.

Figure 9 compares the accretion luminosity predicted by our model for both a black hole (blue region) and

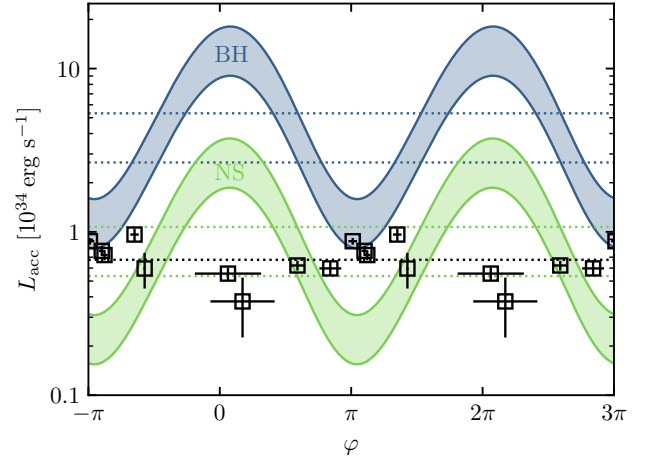


**Figure 9.** Comparison of the accretion luminosity predicted by our model for a black hole (BH; blue region) and a neutron star (NS; green region) accretor in LS 5039 with observational data from Casares et al. (2005). The wind parameters are  $v_\infty = 2440$  km s $^{-1}$  and  $\beta = 0.8$ , and the mass-loss rate ranges from  $\dot{M}_w = 1 \times 10^{-7}$  to  $2 \times 10^{-7} M_\odot$  yr $^{-1}$ . The lower and upper bounds of each shaded region correspond to these limiting values of  $\dot{M}_w$ . The average luminosities for the BH and NS scenarios are  $2.66 \times 10^{34}$  and  $5.36 \times 10^{33}$  erg s $^{-1}$ , respectively. The observed average luminosity is  $6.75 \times 10^{33}$  erg s $^{-1}$ .

a neutron star (green region) accretor with observational data from Casares et al. (2005). The lower and upper bounds of each region correspond to mass loss rates of  $10^{-7}$  and  $2 \times 10^{-7} M_\odot$  yr $^{-1}$ , respectively. The figure shows that the average luminosity for a neutron star accretor ( $5.4 \times 10^{33}$  erg s $^{-1}$ ) agrees better with the averaged observed value than that for a black hole accretor ( $2.7 \times 10^{34}$  erg s $^{-1}$ ).

However, our model predicts a wider range in luminosity ( $L_{\text{max}}/L_{\text{min}} = 8.3$ ) than inferred from observations ( $L_{\text{max}}/L_{\text{min}} = 2.6$ ). Moreover, our model predicts a maximum luminosity around periastron and a minimum around apastron, while the observations suggest the opposite trend. This discrepancy may stem from the fact that our model does not include a detailed treatment of the accretion disk. The reprocessing of accreted material within the disk significantly influences the conversion of mass accretion into luminosity, potentially altering the phase dependence and the range of the observed luminosity (see next subsection).

These findings lend support to the hypothesis that the compact object in LS 5039 is indeed a NS, consistent with previous studies that have suggested a similar conclusion based on X-ray observations (e.g., Makishima et al. 2023). However, further investigations, incorporating a more detailed treatment of the accretion disk physics and radiative processes, are needed to definitively determine the nature of the compact object in LS 5039.

#### 4.2. Caveats

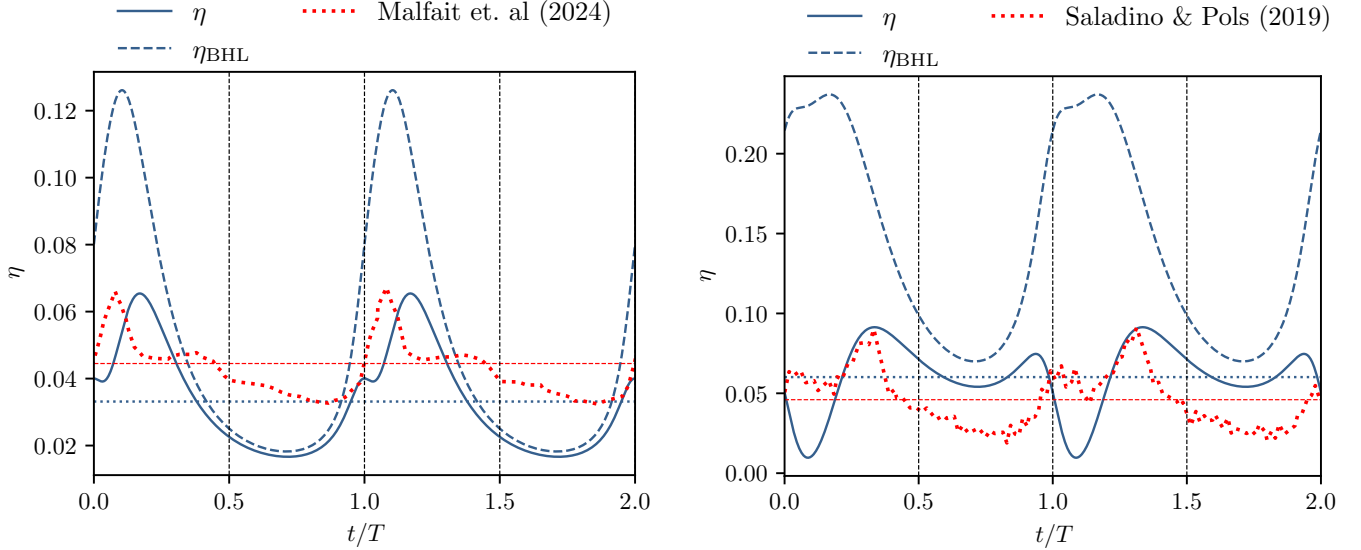


**Figure 10.** Comparison of the mass accretion efficiencies  $\eta$  (solid) and  $\eta_{\text{BHL}}$  (dashed) with estimations from numerical simulations ( $\eta_{\text{sim}}$  - red dotted) for eccentric orbits. The horizontal axis shows time  $t$  in units of the orbital period  $T$ . Vertical dashed lines indicate the location of periastron ( $t = 0$ ) and apastron ( $t = 0.5T$ ). Left: A model with  $e = 0.5$  and  $v_w = 22.8 \text{ km s}^{-1}$  from Malfait et al. (2024). Right: A model with  $e = 0.4$  and  $v_w = 15.1 \text{ km s}^{-1}$  from Saladino & Pols (2019). See further details in Table 1.

While our modified BHL model offers a more accurate and comprehensive description of wind accretion in binary systems, it's essential to acknowledge certain limitations and outline future refinements. In this section, we discuss these caveats, highlight potential avenues for further development, and address discrepancies between our model and existing numerical simulations.

#### 4.2.1. Vanishing mass accretion rate

One key prediction of our model is the complete vanishing of mass accretion efficiency at specific orbital phases for eccentric orbits with sufficiently low wind-to-orbital velocity ratios. However, this prediction relies on an idealized scenario of a smooth and homogeneous wind. In reality, stellar winds are variable and exhibit density and velocity inhomogeneities, which would prevent such a complete cancellation of accretion. Nonetheless, our model suggests that even with these inhomogeneities, systems with high eccentricities and low wind velocities could still exhibit sharp drops in accretion at certain orbital phases. Whether these drops translate into observable features requires further investigation, considering the specific radiative processes and the interaction of the emitted radiation with the circumbinary environment.

Despite these caveats, preliminary analysis of optical spectra from the symbiotic system BX Mon ( $e = 0.45$ ) suggests that its variability can be explained by curves similar to those presented in Figure 7 (Toalá et al., in prep.), providing tentative observational support for our prediction of sharp variations in accretion efficiency for eccentric orbits.

#### 4.2.2. Comparison with simulations

Our model generally shows good agreement with numerical simulations (Table 1). However, some discrepancies arise, and we identify three potential sources:

- 1. Wind acceleration:** We find better agreement with simulations where the wind reaches its terminal velocity before encountering the accretor (e.g., Theuns et al. 1996; de Val-Borro et al. 2009; Huarte-Espinosa et al. 2013; Chen et al. 2020). Larger discrepancies occur when the wind is still accelerating, making it difficult to define a precise wind velocity for comparison. This sensitivity to the wind velocity and acceleration profile, consistent with our findings in Figures 5 and 6, highlights the importance of carefully considering the wind properties when applying our model, especially in scenarios with poorly constrained or highly variable winds.
- 2. Accretion disks:** Our model, based on the BHL formalism, does not account for accretion disks. However, several simulations in Table 1 do model the disk, calculating the accretion rate at a radius much smaller than the characteristic BHL accretion radius  $r_{\text{acc}}$  (Eq. 10). This difference in treatment can lead to discrepancies, as the disk can reprocess the accreted material, potentially modifying the accretion history. Figure 10 compares our model's predictions with simulations from Malfait et al. (2024) and Saladino & Pols (2019), showing that while our model captures the average accretion efficiency well (see Table 1 for comparison between  $\eta$  and  $\eta_{\text{sim}}$ ), the detailed accretion

histories differ. To facilitate more direct comparisons, future simulations could track the accretion history at a radius comparable to  $r_{\text{acc}}$ . This would provide a more straightforward way to assess our model’s accuracy in capturing the time-dependent behavior of the accretion process.

### 3. Inherent limitations and numerical effects:

Numerical simulations are subject to limitations and uncertainties related to numerical resolution, algorithms, and boundary conditions, which could contribute to the observed discrepancies. However, it is also important to note that the level of agreement between our model and simulations (typically within a factor of a few) is similar to that observed for the classic BHL model within its regime of applicability ( $w \gg 1$ ; Hunt 1971; Shima et al. 1985; Ruffert & Arnett 1994), where a dimensionless correction factor ( $\alpha \simeq 1$ ) is often introduced to reconcile the model with simulations. This disparity is attributed to various factors, including accretor’s size, limitations in numerical resolution, the equation of state of the accreting gas, and the inclusion of more complex physical processes.

Overall, while our modified BHL model offers a more accurate description of wind accretion in binary systems by incorporating a geometric correction factor, especially for low wind-to-orbital velocity ratios, it is crucial to acknowledge the remaining discrepancies between our model and numerical simulations. These discrepancies highlight the complex nature of wind accretion and emphasize the need for further investigations to improve both theoretical models and numerical simulations, ultimately leading to a more comprehensive understanding of wind accretion processes in binary systems.

## 5. SUMMARY

We revisited the Bondi-Hoyle-Lyttleton (BHL) accretion model for binary systems, focusing on the regime where the wind velocity  $v_w$  is comparable to or less than the orbital velocity  $v_o$ . By introducing a geometric correction factor, we derived a modified expression for the mass accretion efficiency  $\eta$  that remains physically plausible ( $\eta \leq 1$ ) even for  $w = v_w/v_o \ll 1$ , addressing a key limitation of the classic BHL model.

Our modified model predicts two distinct asymptotic behaviors for circular orbits:  $\eta = q^2/w^4$  for  $w \gg 1$ , recovering the classic BHL scaling, and  $\eta = q^2$  for  $w \ll 1$ , consistent with numerical simulations. This accurate description across the full range of  $w$ , without the need for *ad hoc* adjustments, highlights the strength of our geometrically corrected BHL model.

We applied our model to both symbiotic systems and HMXBs, finding that symbiotic systems exhibit higher accretion efficiencies than HMXBs (Figure 2). Our analysis of eccentric orbits revealed a complex interplay between eccentricity  $e$ , the wind-to-orbital velocity ratio  $w$ , and the wind acceleration parameter  $\beta$ , leading to significant variations in  $\eta$ . Notably, we predict the possibility of sharp drops in accretion at specific orbital phases for sufficiently eccentric systems with low  $w$ , offering a potential observational signature of our model.

Our modified BHL model provides a more accurate and comprehensive framework for understanding wind accretion in binary systems, with implications for stellar evolution, population synthesis, and the interpretation of observational data.

- 1 J.A.T. acknowledges support from the UNAM PAPIIT
- 2 project IN102324. This work has made extensive use of
- 3 NASA’s Astrophysics Data System (ADS).

## REFERENCES

- Abate, C., Pols, O. R., Stancliffe, R. J., et al. 2015, *A&A*, 581, A62
- Alcolea, J., Mikolajewska, J., Gómez-Garrido, M., et al. 2023, in *Highlights on Spanish Astrophysics XI*, ed. M. Manteiga, L. Bellot, P. Benavidez, A. de Lorenzo-Cáceres, M. A. Fuente, M. J. Martínez, M. Vázquez Acosta, & C. Dafonte, 190
- Boffin, H. M. J. 2015, in *Astrophysics and Space Science Library*, Vol. 413, *Astrophysics and Space Science Library*, ed. H. M. J. Boffin, G. Carraro, & G. Beccari, 153
- Boffin, H. M. J., & Jorissen, A. 1988, *A&A*, 205, 155
- Bonačić Marinović, A. A., Glebbeek, E., & Pols, O. R. 2008, *A&A*, 480, 797
- Bondi, H. 1952, *MNRAS*, 112, 195
- Bondi, H., & Hoyle, F. 1944, *MNRAS*, 104, 273
- Bozzo, E., Ducci, L., & Falanga, M. 2021, *MNRAS*, 501, 2403
- Casares, J., Ribó, M., Ribas, I., et al. 2005, *MNRAS*, 364, 899
- Chen, Z., Blackman, E. G., Nordhaus, J., Frank, A., & Carroll-Nellenback, J. 2018, *MNRAS*, 473, 747
- Chen, Z., Ivanova, N., & Carroll-Nellenback, J. 2020, *ApJ*, 892, 110
- Davidson, K., & Ostriker, J. P. 1973, *ApJ*, 179, 585
- de Val-Borro, M., Karovska, M., & Sasselov, D. 2009, *ApJ*, 700, 1148
- Dubus, G., Lamberts, A., & Fromang, S. 2015, *A&A*, 581, A27
- Eadie, G., Peacock, A., Pounds, K. A., et al. 1975, *MNRAS*, 172, 35P
- Edgar, R. 2004, *New Astro. Rev.*, 48, 843
- El-Badry, K., Rix, H.-W., Cendes, Y., et al. 2023, *MNRAS*, 521, 4323

- El Mellah, I., Sundqvist, J. O., & Keppens, R. 2019, *A&A*, 622, L3
- Fortin, F., García, F., Simaz Bunzel, A., & Chaty, S. 2023, *A&A*, 671, A149
- Frank, J., King, A., & Raine, D. J. 2002, *Accretion Power in Astrophysics: Third Edition*
- Hansen, T. T., Andersen, J., Nordström, B., et al. 2016, *A&A*, 588, A3
- Hawcroft, C., Sana, H., Mahy, L., et al. 2024, *A&A*, 688, A105
- Hirai, R., & Mandel, I. 2021, *Publ. Astron. Soc. Australia*, 38, e056
- Hoyle, F., & Lyttleton, R. A. 1939, *Proceedings of the Cambridge Philosophical Society*, 35, 405
- Huarte-Espinosa, M., Carroll-Nellenback, J., Nordhaus, J., Frank, A., & Blackman, E. G. 2013, *MNRAS*, 433, 295
- Hunt, R. 1971, *MNRAS*, 154, 141
- Kissmann, R., Huber, D., & Gschwandtner, P. 2023, *A&A*, 677, A5
- Lamers, H. J. G. L. M., & Cassinelli, J. P. 1999, *Introduction to Stellar Winds*
- Lee, Y.-M., Kim, H., & Lee, H.-W. 2022, *ApJ*, 931, 142
- Liu, Z.-W., Stancliffe, R. J., Abate, C., & Matrozis, E. 2017, *ApJ*, 846, 117
- López-Cámara, D., De Colle, F., Moreno Méndez, E., Shiber, S., & Iaconi, R. 2022, *MNRAS*, 513, 3634
- Makishima, K., Uchida, N., Yoneda, H., Enoto, T., & Takahashi, T. 2023, *ApJ*, 959, 79
- Malfait, J., Siess, L., Esseldeurs, M., et al. 2024, *arXiv e-prints*, arXiv:2408.13158
- Martínez-Núñez, S., Kretschmar, P., Bozzo, E., et al. 2017, *Space Sci. Rev.*, 212, 59
- Merc, J., Gális, R., & Wolf, M. 2019, *Research Notes of the American Astronomical Society*, 3, 28
- Michalitsianos, A. G., Kafatos, M., & Hobbs, R. W. 1980, *ApJ*, 237, 506
- Misra, D., Kovlakas, K., Fragos, T., et al. 2023, *A&A*, 672, A99
- Nagae, T., Oka, K., Matsuda, T., et al. 2004, *A&A*, 419, 335
- Negueruela, I. 2010, in *Astronomical Society of the Pacific Conference Series*, Vol. 422, *High Energy Phenomena in Massive Stars*, ed. J. Martí, P. L. Luque-Escamilla, & J. A. Combi, 57
- Pujol, A., Luna, G. J. M., Mukai, K., et al. 2023, *A&A*, 670, A32
- Ramstedt, S., Vlemmings, W. H. T., Doan, L., et al. 2020, *A&A*, 640, A133
- Reig, P., Ribó, M., Paredes, J. M., & Martí, J. 2003, *A&A*, 405, 285
- Romero, G. E., & Vila, G. S. 2014, *Introduction to Black Hole Astrophysics*, Vol. 876, doi:10.1007/978-3-642-39596-3
- Ruffert, M., & Arnett, D. 1994, *ApJ*, 427, 351
- Ryde, N., Gustafsson, B., Eriksson, K., & Hinkle, K. H. 2000, *ApJ*, 545, 945
- Saladino, M. I., & Pols, O. R. 2019, *A&A*, 629, A103
- Saladino, M. I., Pols, O. R., & Abate, C. 2019, *A&A*, 626, A68
- Saladino, M. I., Pols, O. R., van der Helm, E., Pelupessy, I., & Portegies Zwart, S. 2018, *A&A*, 618, A50
- Shakura, N. I., & Sunyaev, R. A. 1973, *A&A*, 24, 337
- Shima, E., Matsuda, T., Takeda, H., & Sawada, K. 1985, *MNRAS*, 217, 367
- Sokoloski, J. L., & Bildsten, L. 2010, *ApJ*, 723, 1188
- Spiegel, D. N., Giuliani, J. L., J., & Knapp, G. R. 1983, *ApJ*, 275, 330
- Takahashi, T., Kishishita, T., Uchiyama, Y., et al. 2009, *ApJ*, 697, 592
- Theuns, T., Boffin, H. M. J., & Jorissen, A. 1996, *MNRAS*, 280, 1264
- Toalá, J. A., González-Martín, O., Sacchi, A., & Vasquez-Torres, D. A. 2024, *MNRAS*, 532, 1421
- Vink, J. S., & Sander, A. A. C. 2021, *MNRAS*, 504, 2051
- Volkov, I., Kargaltsev, O., Younes, G., Hare, J., & Pavlov, G. 2021, *ApJ*, 915, 61
- Vos, J., Østensen, R. H., Marchant, P., & Van Winckel, H. 2015, *A&A*, 579, A49
- Yoneda, H., Makishima, K., Enoto, T., et al. 2020, *Phys. Rev. Lett.*, 125, 111103
- Zabalza, V., Paredes, J. M., & Bosch-Ramon, V. 2008, *International Journal of Modern Physics D*, 17, 1867
- Zamanov, R. K., Stoyanov, K. A., Marchev, V., et al. 2024, *Astronomische Nachrichten*, 345, e20240036

## APPENDIX

## A. OBSERVED PROPERTIES OF BINARY SYSTEMS

Table A1 provides key observational properties of selected symbiotic and high-mass X-ray binary (HMXB) systems used to exemplify our theoretical model predictions. These systems, characterized by distinct wind velocities and mass accretion properties, are also plotted in the parameter space shown in Figure 2. The data for the symbiotic systems were sourced from the *New Online Database of Symbiotic Variables* (Merc et al. 2019)<sup>1</sup>, while HMXB properties were taken from *A Catalogue of High-Mass X-ray Binaries in the Galaxy From the INTEGRAL to the Gaia era* (Fortin et al. 2023)<sup>2</sup>.

Table A1 also includes the predicted mass accretion efficiencies  $\eta$  and  $\eta_{\text{BHL}}$  computed for each system which, for simplicity, have been computed assuming circular orbits. For symbiotic systems, we assume a typical stellar wind velocity of  $20 \text{ km s}^{-1}$ , with a possible range from  $10$  to  $30 \text{ km s}^{-1}$  (Ramstedt et al. 2020). For OB stars in HMXB systems, a standard velocity of  $2000 \text{ km s}^{-1}$  is adopted, with a range of  $1000$ – $3000 \text{ km s}^{-1}$  (Vink & Sander 2021; Hawcroft et al. 2024).

Notably, with its extended orbital period, *o* Ceti is positioned closer to the HMXB region in Figure 2 due to its relatively low orbital velocity ( $v_o \simeq 5 \text{ km s}^{-1}$ ). The estimated mass accretion efficiency ( $\eta = 2.5 \times 10^{-4}$ ) implies a corresponding mass accretion rate of  $\dot{M}_{\text{acc}} = \eta \dot{M}_w \approx 8 \times 10^{-11} M_{\odot} \text{ yr}^{-1}$ , assuming a mass-loss rate of  $\dot{M}_w = 3 \times 10^{-7} M_{\odot} \text{ yr}^{-1}$  from the late-type star, as reported in Ryde et al. (2000). This value of  $\dot{M}_{\text{acc}}$  is consistent with estimates of  $\lesssim 10^{-10} M_{\odot} \text{ yr}^{-1}$  from Sokoloski & Bildsten (2010).

<sup>1</sup> <https://sirrah.troja.mff.cuni.cz/~merc/nodsv/>

<sup>2</sup> <https://binary-revolution.github.io/HMXBwebcat/>

**Table A1.** Observed properties and estimated mass accretion efficiencies of selected symbiotic and HMXB systems. The columns list, from left to right: mass of the primary (donor), mass of the secondary (accretor), orbital period, mass ratio  $q = m_2/(m_1 + m_2)$ , range of wind-to-orbital velocity ratio  $w = v_w/v_o$ , and calculated mass accretion efficiencies ( $\eta$  and  $\eta_{\text{BHL}}$ ). For symbiotic systems, we assume a typical wind velocity of  $20 \text{ km s}^{-1}$ , while for HMXBs, we take  $2000 \text{ km s}^{-1}$ . These parameters inform the computed  $\eta$  values (Equation 14), which are then compared with theoretical predictions from the classic BHL model  $\eta_{\text{BHL}}$ .

Object	$m_1$ [ $M_\odot$ ]	$m_2$ [ $M_\odot$ ]	$T$ [yr]	$q$	$w$	$\eta$	$\eta_{\text{BHL}}$
<b>Symbiotic stars</b>							
<i>o</i> Cet	2.00	0.65	497.90	0.25	3.84	$2.42 \times 10^{-4}$	$2.50 \times 10^{-4}$
AE Ara	2.00	0.51	2.00	0.20	0.62	$2.15 \times 10^{-2}$	$4.06 \times 10^{-2}$
AG Dra	1.20	0.50	1.51	0.29	0.65	$4.31 \times 10^{-2}$	$7.95 \times 10^{-2}$
AG Peg	2.60	0.65	2.23	0.20	0.59	$2.19 \times 10^{-2}$	$4.30 \times 10^{-2}$
AR Pav	2.00	0.75	1.65	0.27	0.57	$4.27 \times 10^{-2}$	$8.66 \times 10^{-2}$
AX Per	3.00	0.60	1.86	0.17	0.54	$1.67 \times 10^{-2}$	$3.52 \times 10^{-2}$
BF Cyg	1.50	0.40	2.07	0.21	0.69	$2.03 \times 10^{-2}$	$3.57 \times 10^{-2}$
BX Mon	3.70	0.55	3.78	0.13	0.65	$8.34 \times 10^{-3}$	$1.54 \times 10^{-2}$
CH Cyg	2.20	0.56	15.58	0.20	1.20	$6.98 \times 10^{-3}$	$9.10 \times 10^{-3}$
CQ Dra	5.00	0.85	4.66	0.15	0.62	$1.10 \times 10^{-2}$	$2.08 \times 10^{-2}$
EG And	1.46	0.40	1.32	0.22	0.60	$2.51 \times 10^{-2}$	$4.88 \times 10^{-2}$
ER Del	3.00	0.70	5.72	0.19	0.78	$1.39 \times 10^{-2}$	$2.27 \times 10^{-2}$
FG Ser	1.70	0.60	1.78	0.26	0.62	$3.57 \times 10^{-2}$	$6.81 \times 10^{-2}$
KX TrA	1.00	0.41	3.31	0.29	0.89	$2.62 \times 10^{-2}$	$3.94 \times 10^{-2}$
PU Vul	1.00	0.50	13.42	0.33	1.39	$1.28 \times 10^{-2}$	$1.58 \times 10^{-2}$
R Aqr	1.00	0.70	42.40	0.41	1.96	$7.22 \times 10^{-3}$	$8.10 \times 10^{-3}$
RW Hya	1.60	0.48	1.01	0.23	0.53	$3.26 \times 10^{-2}$	$6.98 \times 10^{-2}$
SY Mus	1.30	0.43	1.71	0.25	0.67	$2.95 \times 10^{-2}$	$5.31 \times 10^{-2}$
TX CVn	3.50	0.40	0.55	0.10	0.35	$8.36 \times 10^{-3}$	$2.53 \times 10^{-2}$
V443 Her	2.50	0.42	1.64	0.14	0.55	$1.21 \times 10^{-2}$	$2.50 \times 10^{-2}$
V694 Mon	1.00	0.90	5.28	0.47	0.94	$6.28 \times 10^{-2}$	$9.15 \times 10^{-2}$
V1261 Ori	1.65	0.55	1.75	0.25	0.62	$3.25 \times 10^{-2}$	$6.15 \times 10^{-2}$
Z And	2.00	0.65	2.08	0.25	0.62	$3.14 \times 10^{-2}$	$5.97 \times 10^{-2}$
<b>HMXB</b>							
1E 1145.1-6141	14.00	1.70	0.039	0.11	9.12	$1.66 \times 10^{-6}$	$1.67 \times 10^{-6}$
1FGL J1018.6-5856	22.90	2.00	0.045	0.08	8.19	$1.39 \times 10^{-6}$	$1.40 \times 10^{-6}$
4U 1538-522	20.00	1.18	0.010	0.06	5.26	$3.78 \times 10^{-6}$	$3.85 \times 10^{-6}$
4U 1700-377	46.00	1.96	0.009	0.04	3.89	$6.42 \times 10^{-6}$	$6.63 \times 10^{-6}$
Cen X-3	20.20	1.34	0.006	0.06	4.28	$1.04 \times 10^{-5}$	$1.07 \times 10^{-5}$
Cyg X-1	40.60	21.20	0.015	0.34	4.22	$3.34 \times 10^{-4}$	$3.43 \times 10^{-4}$
EXO 1722-363	18.00	1.91	0.027	0.10	7.40	$2.96 \times 10^{-6}$	$2.99 \times 10^{-6}$
HD 96670	22.70	6.20	0.014	0.21	5.33	$5.33 \times 10^{-5}$	$5.42 \times 10^{-5}$
HD 259440	15.70	1.40	0.869	0.08	24.86	$1.75 \times 10^{-8}$	$1.75 \times 10^{-8}$
IGR J17544-2619	23.00	1.40	0.013	0.06	5.51	$3.36 \times 10^{-6}$	$3.41 \times 10^{-6}$
IGR J18027-2016	20.00	1.50	0.012	0.07	5.60	$4.65 \times 10^{-6}$	$4.72 \times 10^{-6}$
MWC 656	7.80	5.40	0.165	0.41	15.59	$2.81 \times 10^{-6}$	$2.82 \times 10^{-6}$
OA0 1657-415	14.30	1.42	0.029	0.09	8.19	$1.76 \times 10^{-6}$	$1.77 \times 10^{-6}$
SGR 0755-2933	18.50	1.40	0.163	0.07	13.54	$1.46 \times 10^{-7}$	$1.46 \times 10^{-7}$
SS 433	11.30	4.20	0.036	0.27	8.87	$1.15 \times 10^{-5}$	$1.16 \times 10^{-5}$
Vela X-1	26.00	2.12	0.025	0.08	6.41	$3.20 \times 10^{-6}$	$3.24 \times 10^{-6}$